2017

Temperature Dependence of Dynamical Spin Injection in a Superconducting Niobium Thin Film

Tyler S. Townsend
University of Central Florida

TEMPERATURE DEPENDENCE OF DYNAMICAL SPIN INJECTION IN A SUPERCONDUCTING NIOBIUM THIN FILM

by

TYLER S. TOWNSEND

A thesis submitted in partial fulfilment of the requirements
for the Honors in the Major Program in Physics
in the College of Sciences
and in the Burnett Honors College
at the University of Central Florida
Orlando, Florida

Summer Term, 2017

Major Professor: Enrique del Barco, Ph.d

ABSTRACT

Spintronics is a research field that focuses on the manipulation of the quantum mechanical spin of charge carriers in solid state materials for future technological applications. Creating large spin currents with large relaxation times is sought after in the field of spintronics which may be aided by combining spintronics with superconductivity. This thesis provides a phenomological study of the effective change in ferromagnetic resonance linewidth, ΔH, by dynamical spin injection into a permalloy-copper-niobium tri-layer in the superconducting state. The ferromagetic resonance linewidth was measured from 2-14 K. It was observed that there was a change in the behavior of the resonance as well as a change in the linewidth from the between 6-8 K. An observed change in the resonance field, H_r, shows a clear non monotonic behavior as a function of temperature below 7-8 K. The decrease in linewidth was attributed to the suppression of the spin sinking mechanisms due to the superconducting state of niobium.

DEDICATION

Dedicated to my mother, father, and sister
for their love, encouragement,
and for always understanding.

ACKNOWLEDGMENTS

I would like to thank the many people whom I have encountered during my undergraduate research that have helped me in anyway of completing this thesis. I would like to thank the many members of the del Barco research group that I have worked with: Alvar Rodriquez Garrigues, Jim Atkinson, Marta Anguera Antoñana, Rebecca Cebulka, Priyanka Vaidya, Cameron Nickle, Gyan Khatri, Christopher Coleman, and Jonathan Sepulveda.

Also, I would like to take the time to acknowledge the many people that I have met within the physics department that made my undergraduate experience an enjoyable one :Dr. Lee Chow, Dr. Elena Flitsiyan, Dr. Richard Klemm, Dr. Slava Kokoouline, Dr. Eduardo Mucciolo, Dr. Patrick Schelling, Monika Crittenden, Shelley Glaspie, and Elizabeth Rivera.

Importantly, I would like thank my gracious advisor Dr. Enrqiue del Barco for guidance, and the effort he has put into this project. By his consideration, I was given an opportunity to work in his lab which led me to change my major to physics. I would like to show appreciation for the efforts of Dr. Coffey and his group for fabricating the materials, and I would also like to thank support from the ECCS Engineering Division of the National Science Foundation.

Lastly, I would like to thank Dawn Townsend, John Townsend, Roberta Townsend, and Abbey Townsend. Their support for my education has been cherished; I owe the completion of this thesis and my undergraduate education to their encouragement.

TABLE OF CONTENTS

LIST OF FIGURES

CHAPTER 1: INTRODUCTION

1.1 Spintronics

Spintronics is an emerging multidisciplinary area of research that focuses on the manipulation of the electron's spin so that it may be used for novel technologies (Figure 1). These technologies would make use of spin currents as opposed to traditional charge currents. Spintronics is deemed to be a highly active research area with promising applications. Since the discovery of the giant magnetoresistance effect, spintronics has already found applications in hard disk drive read heads [1]. Fundamental studies within the field of spintronics include investigating the interaction between the particle's spin and its solid-state environment along with understanding the spin dynamics and spin relaxation mechanisms within the solid [2].

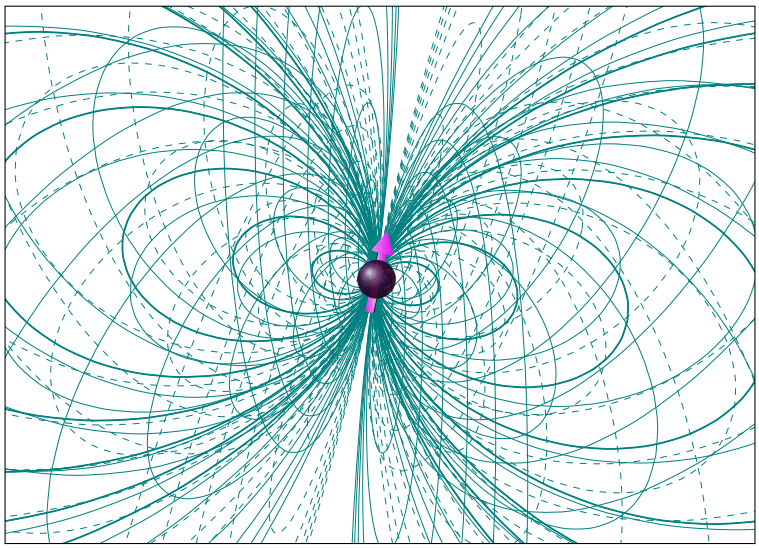

Figure 1.1: The electron possesses an intrinsic property called spin. The magnetic moment of an electron proceeds from its spin. The manipulation of the electron's spin is an endeavor for future spintronic applications.

Spintronics provides faster and more efficient logic operations controlled by spin currents, as op-

posed to the charge-based logic operations in semiconductors, [1]. Several techniques are available to generate *pure* spin currents, such as non-local spin injection, optical injection from circularly polarized light, non-local spin injection, and spin-pumping from the precessing magnetization of a ferromagnet (FM) [3]. Pure spin currents do not generate a net charge current, and as a consequence, stray Oersted fields shall be absent from devices employing pure spin current. In order to advance the field of spintronics, efficient generation and manipulation of spin currents in a solid remains a key requirement for future spintronic devices and applications so that information may be carried, transported, and processed [4, 1]. This may be accomplished by combining superconductivity with spintronics.

1.2 Superconducting Spintronics

Superconductors (SC) are anticipated to show many fascinating phenomena when combined with spintronics. Enhanced spin lifetimes in the superconducting state have already been demonstrated. Wakamura et. al found that the intrinsic spin relaxation time in superconducting Niobium (Nb) was four times greater than in the normal conducting state [5]. Spin transport in superconductors is generated by superconducting quasiparticles as opposed to the normal metal (NM) electrons [5].

Typically, Cooper pairs, the charge carriers in SC as opposed to electrons, have a spin, S=0, so they do not absorb spin angular momenta. However, since the prediction of the Cooper pair spin triplet state in FM/SC hybrids in 2001, FM/SC heterostructures have been studied extensively by examining proximity effects in order to find a powerful method to form and manipulate superconducting spin triplet pairs [6, 7, 8]. From a study of the Josephson effect in SC/FM/SC junctions, ferromagnetic spin dynamics have been identified to have a strong influence on the SC system [13]. SC/FM/SC are intriguing structures which have garnered a lot of attention since the SC/FM/SC π-junctions were proposed as potential logic elements in quantum computing circuits [12]. One

paper suggests that in a FM/NM/SC, where NM stands for normal-metal, the odd-frequency pairing of the spin triplet ($S_z = \pm 1$) induced in the NM layer is altered by changing the precessional frequency of the FM by spin pumping [13].

Despite many theoretical works in SC/FM systems and its potential applications, there is still a need for experimental work in the field [1]. These systems have not been explored as much experimentally utilizing pure spin currents [9]. The first study on spin injection into a superconductor showed a strong reduction in the spin-flip length, λ_{sf}, below the transition temperature. This was attributed to proximity effects and strong Andreev processes [10]. It was also found that in superconducting Nb, the SC strongly suppresses spin absorption implying the SC is an insulator for pure spin current [11]. A previous work with a FM/SC system measured the change in linewidth as a function of temperature by dynamical spin injection. They attributed the change in linewidth as a suppression of the spin sink efficiency of Nb (the SC) in the superconducting state. Furthermore, they also suggest that the proximity effect penetrates the entire ferromagnetic layer instead of a small region [14].

The ultimate goal of using polarized spin supercurrents relies on experiments forming and manipulating superconducting triplet pairs in these hybrid structures [8]. This creates an interesting opportunity to experimentally explore spin dynamics in an FM/NM/SC system.

1.3 Thesis Outline

Although effort has been put into understanding spin triplet creation and manipulation in the FM/SC systems, the spin dynamics in a FM/NM/SC have yet to be fully understood [1, 13]. Additionally, the superconducting spin sinking efficiency has not eliminated proximity effects in previous FMR studies to assert Cooper pair formation as the mechanism behind the decrease

spin angular momentum transfer. This paper presents a phenomenological study of the spin dynamics in a FM/NM/SC system via spin pumping. This experiment will implement a permalloy/copper/niobium (Py/Cu/Nb) layer as a means to measure the FMR response as a function of temperature. Permalloy is chemically defined as ($Fe_{20}Ni_{80}$).

Niobium is known to have a transition temperature of 9.3 K, the highest of all natural elements [16]. There have been extensive, superconducting spin transport studies on Nb, and Nb's high transition temperature and strong spin-orbit coupling make Nb very desirable for low temperature experiments [9, 11, 14, 15]. The strong spin orbit coupling of Nb has shown phenomena such as the spin Hall effect which makes detection of the spin transport possible [15]. It has also been shown that a copper spacer separating the superconducting and ferromagnetic layers eliminates the proximity effect. A recent study reported that the spin relaxation process in the Cu layer is not affected by the proximity effect from Nb in the superconducting state [11]. This study of spin pumping in Py/Cu/Nb will eliminate proximity effects seen in the Py/Nb spin pumping study done by Bell et al. [14] to underline the mechanism behind the change in FMR linewidth.

This paper shall present a brief overview of the main topics covered in this experiment including the theory of the FMR, theory of spin pumping, spin-orbit coupling in solids and its observed effects, and the interplay between SC/NM and SC/FM interfaces. Chapter 3 contains a detailed overview of the experiment carried out in this thesis project including the devices used, fabrication processes, the setup, and the experimental procedure. Chapter 4 shows the results from the two experiments (a Py/Cu/Nb sample and a Py sample for comparison) along with an analysis of the anomaly observed in their behavior. The final chapter includes the future outlook for other experiments and the implications of this work.

CHAPTER 2: LITERATURE REVIEW

2.1 Ferromagnetic Resonance (FMR)

Ferromagnetism classifies the magnetic behavior of certain materials (such as iron). They are known as permanent magnets and for their strong attraction to other magnets. The spontaneous magnetization resulting from the parallel alignment of quantum spins is the origin of this behavior. The resonance condition of ferromagnetism may be interpreted classically, and quantum-mechanically. The resonance condition arises at a quantum level when the electronic moments are split by a uniform magnetic field with electromagnetic radiation applied at the frequency, ω, corresponding to the difference between the split energy levels $\Delta E = \hbar\omega$, where $\hbar$ is the reduced Planck constant. This resonance occurs classically when the oscillating field is applied at the Lamor frequency [17]. Due to the correspondence principle, the theory of ferromagnetic resonance may be obtained by a classical approximation [18].

The d-electrons are responsible for the ferromagnetic coupling between atoms in transition metals [17]. Each of these atoms have a magnetic moment which can be described classically as

$$\boldsymbol{\mu} = -\frac{e}{2m_e}\mathbf{L} \tag{2.1}$$

$$= -\gamma\mathbf{L} \tag{2.2}$$

where $\gamma = e/2m_e$ is the magneto-mechanical ratio, e is the charge of the electron, and m_e is the non-relativistic mass of the electron. By taking the time derivative of Equation 2.2, the following equation is obtained:

$$\frac{d\boldsymbol{\mu}}{dt} + \gamma\frac{d\mathbf{L}}{dt} + \mathbf{L}\frac{d\gamma}{dt} = 0 \tag{2.3}$$

which γ may be taken as constant; hence, $d\gamma = 0$. Equation (2.3) may then be rearranged as

$$\frac{1}{\gamma}\frac{d\boldsymbol{\mu}}{dt} = -\frac{d\mathbf{L}}{dt} = -\boldsymbol{\Gamma} \tag{2.4}$$

where $\boldsymbol{\Gamma}$ is the torque exerted. The torque $\boldsymbol{\Gamma} = \mu \times \mathbf{H}_{\text{ext}}$ is a result of the electron being placed in an applied magnetic field, $\mathbf{H}_{\text{ext}}$, which the moment, $\boldsymbol{\mu}$, will attempt to align with $\mathbf{H}_{\text{ext}}$. Equation 2.4 may be written in terms of the $\mathbf{H}_{\text{ext}}$ as

$$\frac{1}{\gamma}\frac{d\boldsymbol{\mu}}{dt} = -\boldsymbol{\mu} \times \mathbf{H}_{\text{ext}}. \tag{2.5}$$

Typically, magnetic materials contain a large number of magnetic moments, so the total atomic magnetic moment is magnetization vector, $\mathbf{M}$, given by $\mathbf{M} = N\boldsymbol{\mu}$. Equation 2.5 may now be written as

$$\frac{1}{\gamma}\frac{d\mathbf{M}}{dt} = -\mathbf{M} \times \mathbf{H}_{\text{ext}}. \tag{2.6}$$

Equation 2.6 describes the equation of motion for a magnetic moment, that sweeps out a cone rotating about the axis parallel to $\mathbf{H}_{\text{ext}}$ at angle θ, given that $\mathbf{H}_{\text{ext}}$ is constant. $\mathbf{M}$ precesses about $\mathbf{H}_{\text{ext}}$ at a frequency $\omega = \gamma H_{\text{ext}}$, called the Larmor frequency.

In real ferromagnets, damping is present; consequently, the magnetization will eventually align along the equilibrium axis (parallel to the magnetic field) [19]. The Landau-Lifshitz-Gilbert (LLG) equation accurately describes the response of the ferromagnetic resonance in both bulk and thin-film materials [20]. The LLG equation is described as

$$\frac{d\mathbf{M}}{dt} = -\gamma\mathbf{M} \times \mathbf{H}_{\text{eff}} + \frac{\alpha}{M_s}\mathbf{M} \times \frac{d\mathbf{M}}{dt} \tag{2.7}$$

where $\mathbf{M}$ is the magnetization vector, $d\mathbf{M}/dt$ is the rate of change of the magnetization, M_s is the

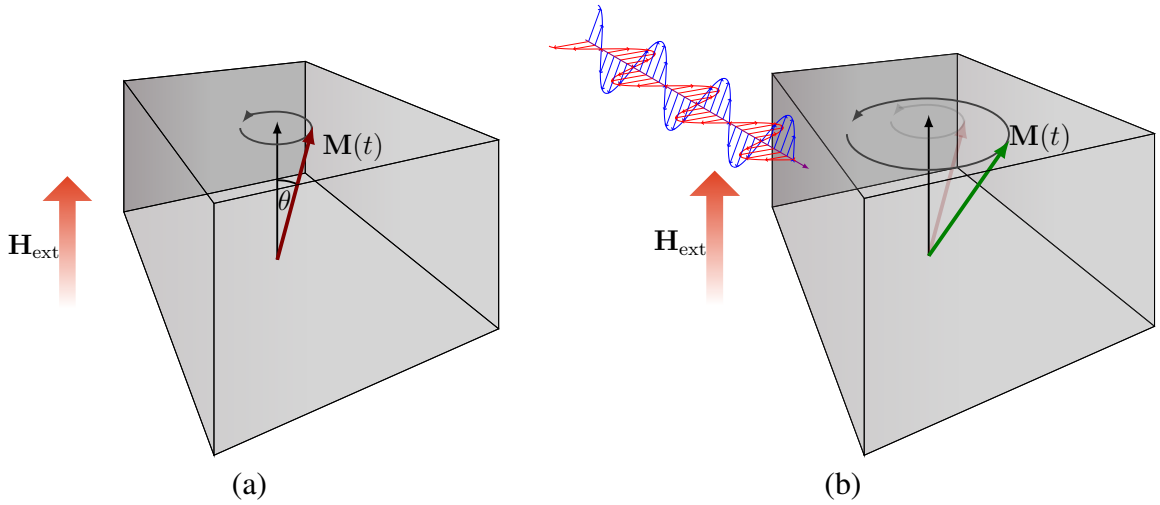

Figure 2.1: (a) When an external magnetic field is applied to a ferromagnetic material, the magnetization of the material will precess about the axis perpendicular to the applied field. (b) When electromagnetic radiation is applied to the material matching the resonance frequency, the magnetization becomes excited and precesses continuously around the equilibrium axis.

saturation magnetization of the material, α is the Gilbert damping parameter, $\gamma = g\mu_B/\hbar$ is the gyromagnetic ratio, μ_B is the Bohr magneton, g, is the Landé g-factor, $\hbar$ is the reduced Planck's constant, and $\mathbf{H}_{\text{eff}}$ is the effective magnetic field from the external field and the internal field inside the ferromagnet. There is one approximation that is necessary to derive the LLG equation and that is the adiabatic assumption that the frequency, ω, of the magnetization is slow compared to the internal exchange splitting energies which holds for most ferromagnets [20].

The overview of the FMR condition can be seen in Figure 2.1(b). The constant, external field is applied to the ferromagnetic and the electromagnetic radiation produces an alternating current (a.c.) magnetic field H_{ac}. Typically, this magnetic field is applied perpendicularly to the H_{ext}. Employing the radiation at the frequency of the magnetization precession, ω, the precession of the magnetization is enhanced due to the energy and angular momentum absorbed [19]. In order to delineate this, take the effective magnetic field as $\mathbf{H}_{\text{eff}} = (H_{\text{ac}}\cos(\omega t), H_{\text{ac}}\sin(\omega t), H_{\text{ext}})$, where $\omega = \gamma H_{\text{ext}}$ is the resonance frequency, and the magnetic anisotropy of the material is neglected to

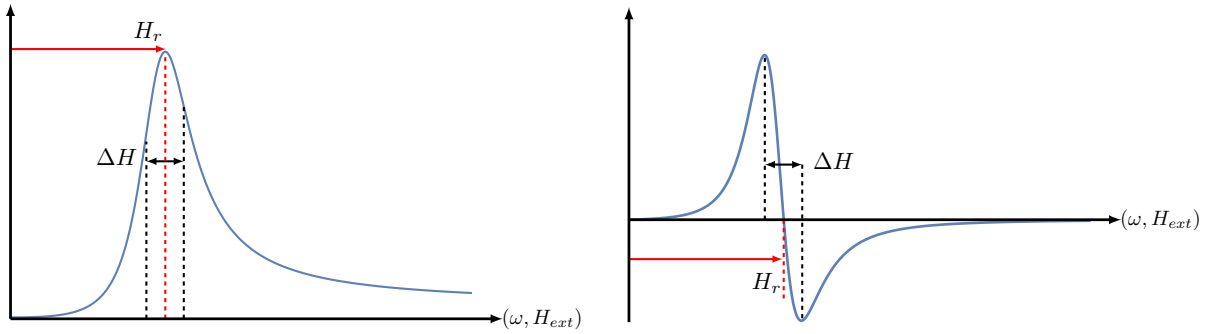

(a) (b)

Figure 2.2: (a) The Lorenzian curve described by Equation (2.9). (b) The derivative of the Lorenzian with respect to the applied field. Both curves have two parameters along the abscissa. Theoretically, ω, is used as the microwave frequency is varied with a constant magnetic field. Experimentally, the setup is much easier by fixing the microwave frequency and varying the magnetic field where H. $H_{\text{eff}} = H_r$ is the resonance condition. This is described in Section 3.3

simplify the problem. The power absorbed is

$$\mathcal{P} = \frac{1}{T}\int \mathbf{H}_{\text{eff}} \cdot d\mathbf{M} = 2\omega H_{\text{ac}}^2 \chi'' \tag{2.8}$$

where $T = 2\pi/\omega$ is the period of precession of the magnetization and

$$\chi'' = \frac{\alpha\omega}{2[(\gamma H_{\text{ext}} - \omega)^2 + (\alpha\omega)^2]} \tag{2.9}$$

is the imaginary part of the magnetic susceptibility [19]. Equation (2.9) has the form of a Lorenzian (Figure 2.2(a)), so the absorbtion spectrum would be of the same shape. Experimentally, it is fundamental to fix the frequency of microwave radiation and vary the strength of the external field across the resonance condition. By doing so, the derivative of Equation (2.9) with respect to $\mathbf{H}_{\text{eff}}$ ($\partial P/\partial H_{\text{eff}}$) can be taken which exhibits two peaks (Figure 2.2(b)). The peak to peak separation, ΔH, is the line width expressed as

$$\Delta H = \frac{2\omega}{\sqrt{3}\gamma}\alpha. \tag{2.10}$$

This precession of the FM induces spin-pumping into a NM which causes an increase in the effective Gilbert damping constant. This is discussed in the next section.

2.2 Dynamical Spin Pumping

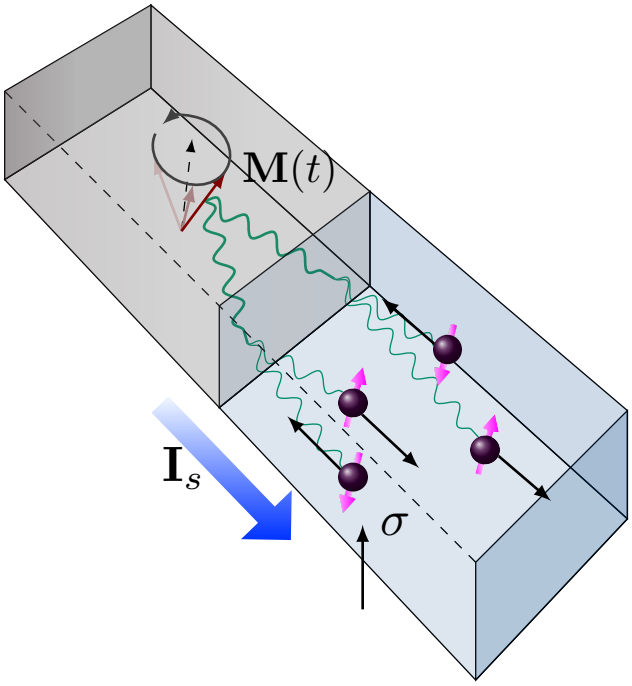

Figure 2.3: A diagram portraying the process of spin pumping. As the magnetization, $\mathbf{M}$, precesses, the exchange interaction at the interface transfers spin angular momentum from the FM to the NM. This drives a spin current into the FM as electrons of opposite spin populate opposite sides of the NM. Here $\mathbf{I}_s$ is the spin current, $\boldsymbol{\sigma}$ is the spin polarization vector.

Spin pumping relies on the precession of the magnetization in the FM induced by the FMR condition (Figure 2.3). The theory of spin pumping is outlined by following references [20, 21, 22]. Consider an FM/NM junction as seen in Figure 2.4. Under the application of an external magnetic field, $\mathbf{H}_{\text{eff}}$, the direction of the magnetization in the ferromagnet begins precessing. The magnetic field is assumed to be applied along the z-axis. The precession of the magnetization vector, $\mathbf{M}(t)$, pumps the spin current, $\mathbf{I}_s^{pump}$, out of the ferromagnet into the normal layer NM by dynamic ex-

change coupling at the interface [23]. The current pumped into the normal layer is dependent upon the spin-pumping conductance, $\mathcal{A} \equiv \mathcal{A}_r + i\mathcal{A}_i$, which is given by the following relationship:

$$\mathbf{I}_s^{\text{pump}} = \frac{\hbar}{4\pi}\left(\mathcal{A}_r \mathbf{m} \times \frac{d\mathbf{m}}{dt} - \mathcal{A}_i \frac{d\mathbf{m}}{dt}\right) \tag{2.11}$$

where $\mathbf{m} = \mathbf{M}/|\mathbf{M}|$ and $d\mathbf{m}/dt$ are the unit vectors of the magnetization and the rate of change of the direction of the magnetization, respectively. The terms $\mathcal{A}_{r,i}$ are the real and imaginary parts of the spin-pumping conductance. The spin-pumping conductance written in terms of transmission and reflection coefficients is

$$\mathcal{A} = g^{\uparrow\downarrow} - t^{\uparrow\downarrow} \tag{2.12}$$

where $g^{\uparrow\downarrow}$ is the dimensionless conductance matrix and $t^{\uparrow\downarrow}$ is the transmission matrix. If the transverse spin-coherence length is smaller than the thickness of the ferromagnetic film, then the spin pumping is governed by the interfacial mixing conductance, that is $\mathcal{A} = g^{\uparrow\downarrow}$ [21].

When spin is pumped into the NM, backflow of the spin current may enter the FM from spin accumulation. The net spin current of the system is

$$\mathbf{I}_s = \mathbf{I}_s^{\text{pump}} - \mathbf{I}_s^{\text{back}} \tag{2.13}$$

where $\mathbf{I}_s^{\text{back}}$ is the back flow back into the ferromagnet from spin accumulation. If the NM is an ideal spin sink, the back flow is neglected ($\mathbf{I}_s^{\text{back}} \sim 0$), as the spins are assumed to dissipate completely through spin-flip processes [22]. Then the spin flow is completely driven by spin pumping alone ($\mathbf{I}_s \sim \mathbf{I}_s^{\text{pump}}$).

The spin current generated at the interface FM/NM accumulates a spin density $\boldsymbol{\mu}_s$ inside the NM layer. $\boldsymbol{\mu}_s = \boldsymbol{\mu}^{\uparrow} - \boldsymbol{\mu}^{\downarrow}$, is the electro-chemical potential difference between up and down spins, also known as the spin accumulation energy [3]. The accumulation of spins will have a spatial

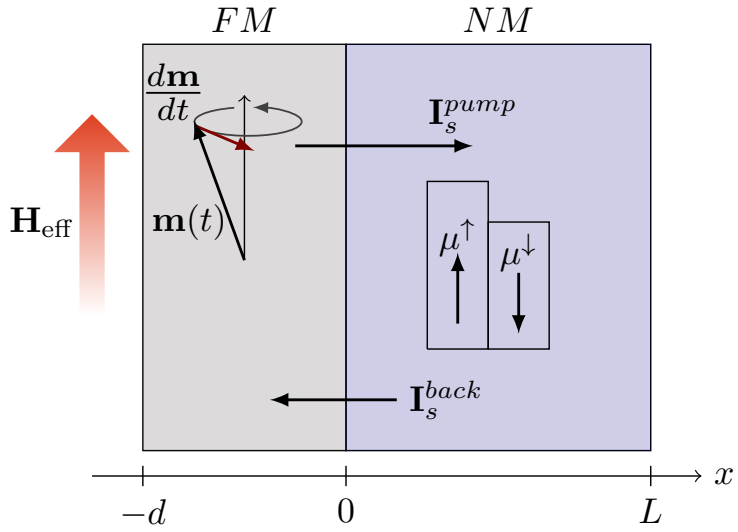

Figure 2.4: Diagram of spin pumping in a FM/NM structure. The application of $\mathbf{H}_{\text{eff}}$ is taken to be along the z-axis. This causes magnetization to precess along the path of the gray vector. The change in the direction of $\mathbf{m}(t)$ is given by $d\mathbf{m}/dt$ indicated by the red vector. At the interface spin current is pumped into the NM $\mathbf{I}_s^{\text{pump}}$. Due to spin accumulation at some x, there is a back-flow of spin current, $\mathbf{I}_s^{\text{back}}$, that is driven back into the FM. $\mu^{\uparrow}$ and $\mu^{\downarrow}$ are the electro-chemical potentials of the spin up and spin down states in the metal, respectively. The difference between $\mathbf{I}_s^{\text{pump}}$ and $\mathbf{I}_s^{\text{back}}$ is the net spin current.

dependence from the interface described by

$$i\omega\boldsymbol{\mu}_s(x) = D\frac{\partial^2}{\partial x^2}\boldsymbol{\mu}_s(x) - \tau_{sf}^{-1}\boldsymbol{\mu}_s(x) \tag{2.14}$$

where ω is the the angular frequency of the precession, τ_{sf} is the spin-flip rate, and D is the diffusion coefficient. The boundary conditions are determined by the the continuity of the spin current from the FM into the NM [22]

$$\begin{aligned} \frac{\partial}{\partial x}\boldsymbol{\mu}_s(0) &= -2(\hbar\mathcal{N}SD)^{-1}\mathbf{I}_s^0 \\ \frac{\partial}{\partial x}\boldsymbol{\mu}_s(L) &= 0 \end{aligned} \tag{2.15}$$

where $\mathbf{I}_s^0 \equiv \mathbf{I}_s(x=0)$, $\mathcal{N}$ is the one-spin density of states in the film, and $\mathcal{S}$ is the surface area of

the FM/NM interface. Solving the diffusion equation with boundary coefficients, the solution is

$$\boldsymbol{\mu}_s(x) = \frac{\mathbf{I}_s^0}{k}\frac{\cosh k(x-L)}{\sinh(kL)}\frac{2}{\hbar\mathcal{N}SD} \tag{2.16}$$

where the wave vector, k, is given by $k = 1/\lambda_{sd}\sqrt{1+i\omega\tau_{sf}}$ and $\lambda_{sd} = \sqrt{D\tau_{sf}}$ is the spin-flip diffusion length in the NM [21]. Since the net spin current is proportional to the gradient of the spin accumulation at the FM/NM interface [24], the spin current may be written as[3],

$$\mathbf{I}_s(x) \propto \frac{\partial}{\partial x}\boldsymbol{\mu}_s(x) = \mathbf{I}_s^0\frac{\sinh k(x-L)}{\sinh(kL)}\frac{2}{\hbar\mathcal{N}SD}. \tag{2.17}$$

The instantaneous spin current at the FM/NM interface is proportional to the real part of the interfacial spin-mixing conductance, $g_r^{\uparrow\downarrow}$, given by the following relationship [26],

$$I_s^0 = \frac{\omega}{2\pi}\int_0^{2\pi/\omega} g_r^{\uparrow\downarrow}\frac{\hbar}{2\pi}\frac{1}{M_s^2}\left(\mathbf{M}(t)\times\frac{d\mathbf{M}(t)}{dt}\right)_z dt \tag{2.18}$$

where $\left(\mathbf{M}(t)\times d\mathbf{M}(t)/dt\right)_z$ is the z component of $\mathbf{M}(t)\times d\mathbf{M}(t)/dt$. The efficiency of spin pumping across the interface is given by the spin-mixing conductance [25],

$$g_r^{\uparrow\downarrow} = \frac{2M_s d}{\gamma\hbar}(\alpha_{FM/NM} - \alpha_{FM}) \tag{2.19}$$

where $\alpha_{FM/NM}$, α_{FM} are the Gilbert damping coefficients for the FM/NM stack, and the FM alone, respectively. It is obvious from Equation 2.18, that the injected spin current is proportional to the real part of the spin-mixing conductance which is also determined by the enhanced damping from Equation 2.19. So from Equation 2.10, the enhanced broadening of the FMR spectrum (the linewidth of the Lorenzian) can be attributed to spin-pumping.

Extending the theory of spin pumping into a FM/NM_1/NM_2 tri-layer material, spins are pumped

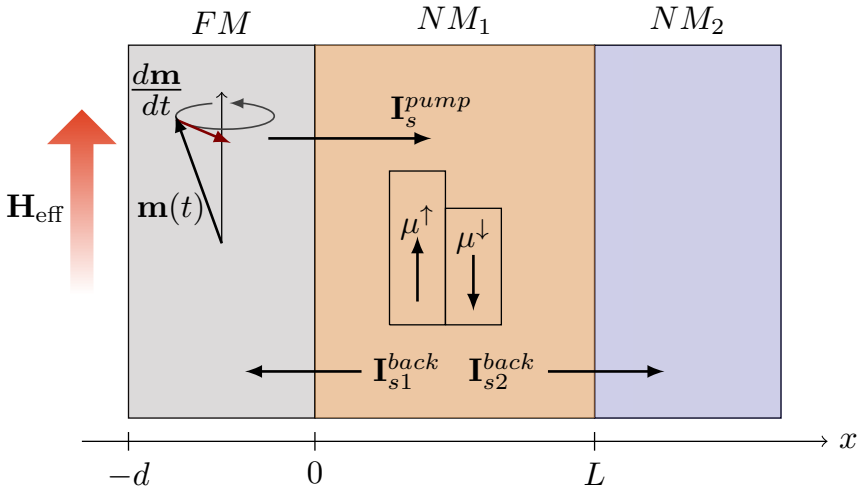

Figure 2.5: In a FM/NM/NM system, spin current is injected in the first NM from the FM. The accumulation of spin in NM_1 will allow dispersion into the FM, $\mathbf{I}_{s1}^{back}$, and into NM_2, $\mathbf{I}_{s2}^{back}$.

into N_1, which allows for the possibility of the spins to reach the second normal metal or diffuse back into the FM [21]. The boundary conditions for the diffusion equation now become

$$\begin{aligned} \frac{\partial}{\partial x}\boldsymbol{\mu}_s(0) &= -2(\hbar\mathcal{N}SD)^{-1}\mathbf{I}_s^1 \\ \frac{\partial}{\partial x}\boldsymbol{\mu}_s(L) &= -2(\hbar\mathcal{N}SD)^{-1}\mathbf{I}_s^2 \end{aligned} \tag{2.20}$$

where $\mathbf{I}_s^1$ and $\mathbf{I}_s^2$ are the total spin currents through the FM/NM_1 interface and the NM_1/NM_2 interface, respectively. Now there is a spin accumulation in NM_1, therefore $\mathbf{I}_s^1$ now includes contributions from $\mathbf{I}_s^{\text{pump}}$ as well as $\mathbf{I}^{\text{back}}$. The spin current into NM_2 is now driven by the NM_1 spin-accumulation [21]

$$\mathbf{I}_s^2 = \frac{g}{4\pi}\boldsymbol{\mu}_s(L) \tag{2.21}$$

where g is the conductance per spin at the NM_1/NM_2 interface. This configuration will model the Py/Cu/Nb sample. Copper is considered a poor spin sink [23], while niobium exhibits strong-spin orbit coupling which makes it a good spin sink [5]. The following section will explain spin orbit

coupling in spin dynamics.

2.3 Spin-Orbit Interaction

The spin-orbit interaction has been described as the source of most of the relaxation mechanisms for spin transport [2]. The Gilbert damping in transition-metals is thought to be from the spin-orbit interaction due impurity scattering [20]. In hydrogen-like atoms, the spin-orbit interaction arises from the central force contribution from the potential for the valence electrons. This electric potential is $V(\mathbf{r}) = e\phi(\mathbf{r})$ where e is the electron charge and $\phi(\mathbf{r})$ is an arbitrary scalar potential. $V(\mathbf{r})$ is not the Coulomb potential because of electron-electron interaction in higher orbitals. The valence electron then encounters the electric field $\mathbf{E} = -(1/e)\nabla V(\mathbf{r})$. As it moves from the electric field, it "feels" an effective magnetic field [27],

$$\mathbf{B}_{\text{eff}} = -\frac{\mathbf{v}}{c} \times \mathbf{E} = -\frac{\mathbf{v}}{c} \times \frac{-1}{e}\frac{\partial V_r}{\partial r}\hat{\mathbf{r}} \tag{2.22}$$

where $\mathbf{v}$ is the velocity of the electron and c is the speed of light. This magnetic field will try to align the intrinsic moment of the electron along the direction of the field. The Hamiltonian is

$$\hat{H} = -\boldsymbol{\mu}_{spin} \cdot \mathbf{B}_{\text{eff}}. \tag{2.23}$$

The intrinsic magnetic moment of the electron is given by

$$\boldsymbol{\mu}_{spin} = \frac{e\mathbf{S}}{m_e c} \tag{2.24}$$

where m_e is (again) the mass of the electron. The Hamiltonian now becomes

$$\hat{H}_{L\cdot S} = -\frac{e\mathbf{S}}{m_e c}\left(\frac{\mathbf{p}}{m_e c} \times \left(\frac{\mathbf{r}}{er}\right)\frac{\partial V_r}{dr}\right) = \frac{1}{m_e^2 c^2}\frac{1}{r}\frac{\partial V_c(r)}{\partial r}(\mathbf{S}\cdot\mathbf{L}) \tag{2.25}$$

According to Equation 2.25, the spin and the motion of the electron are coupled by the $(\mathbf{S}\cdot\mathbf{L})$ term; however, it does not accurately depict the spin-orbit interactions in solids. One intriguing phenomenon derived from the spin-orbit interaction is the spin Hall effect (SHE). The SHE arises when spin-dependent scattering couples the electric current in a conducting material to generate a spin current. There are two different mechanisms that generate the SHE in materials. One is electron spin-dependent impurity scattering, which is known as the extrinsic SHE. The other is due to the band's Berry phase, known as the intrinsic SHE [28, 29]. This effect can generate a spin current without the need of a magnetic field, see Figure 2.5 [3].

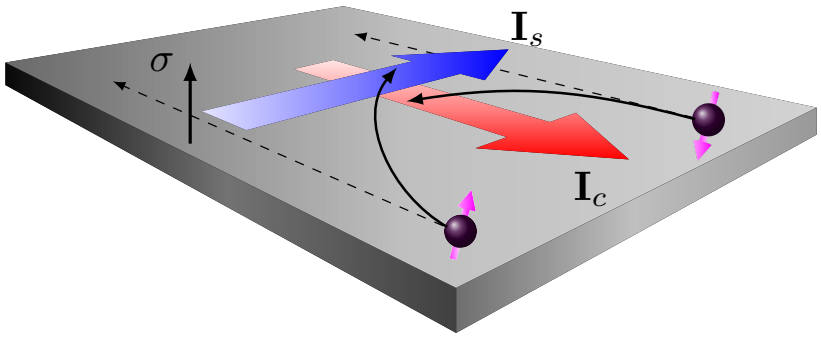

Figure 2.6: The spin Hall effect converts a charge current,$\mathbf{I}_c$, into a spin current,$\mathbf{I}_s$. The diagram illustrates electrons moving to the lateral edges of the material due to the spin-orbit effect generating a spin current $\mathbf{I}_s$. $\boldsymbol{\sigma}$ denotes the spin-polarization vector for the spin current.

The first predictions of the SHE date back to 1970 when it was predicted that the spin of electrons would spatially align themselves due to the spin-orbit interaction [31, 32]. It was not until 2004 that the first observations of the SHE were seen in semiconductors [33], and then in metals in 2006 [29]. Conversely, a net charge current could be obtained from a pure spin current, an effect known

as the inverse spin Hall effect (ISHE). The ISHE converts a spin current into a charge current through the aforementioned same spin-orbit interactions.

When two electrons of opposite spins travel in an anti-parallel fashion, they generate a spin current. The spin orbit interaction will bend two opposite spin polarized electrons into the same direction. This will induce a potential difference, creating a charge current as seen in Figure 2.6. The charge current conversion is known as the ISHE which can be described as follows [28],

$$\mathbf{I}_c \propto \mathbf{I}_s \times \boldsymbol{\sigma} \tag{2.26}$$

where $\boldsymbol{\sigma}$ is the spin polarization of the system. This shows that the observed ISHE signal is directly proportional to the spin injected current.

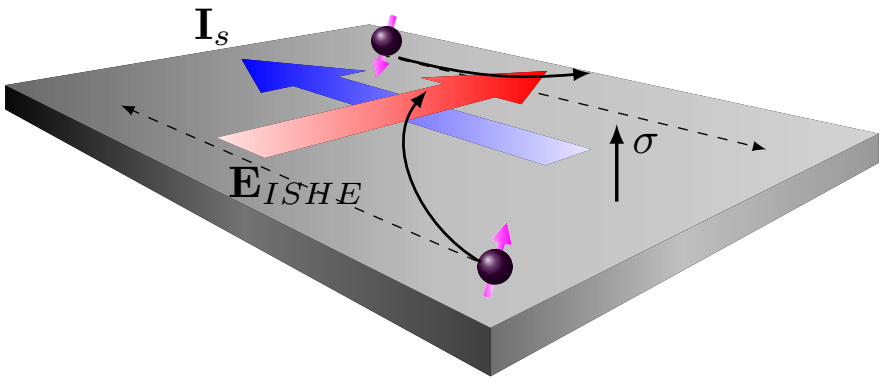

Figure 2.7: When a metal exhibits the spin Hall effect, generating a spin current in a material will cause the electrons to deflect to the same side of material creating an unequal population of electrons generating a Hall voltage. This allows for electrical detection of the spin current in the material.

Since the SHE is a consequence of spin-dependent scattering, materials with large spin-orbit coupling are favorable for the generation of spin currents and desirable for spintronic devices [30]. The SHE in 4d and 5d transition metals such as Nb are more difficult to measure due to their short spin diffusion lengths [30]. Recently, the SHE has been demonstrated in a superconducting niobium nitride (NbN) layer with the ISHE signal enhanced by 2000 times the normal conducting signal

(NC) [5].

The increase of the ISHE in superconducting materials is highly surprising. One would expect exactly the opposite behavior according to the nature of electrical carriers responsible for the supercurrent, i.e. the Cooper pairs, with opposite paired spins, and thus unable to take a net spin angular momentum. Wakamura et al. of reference [5] describe spin transport in superconductors due to quasiparticles which makes the study of dynamical spin pumping in superconducting Nb of high interest.

2.4 Superconductivity in FM/SC and NM/SC Systems

Charge transport in superconductors is carried out by Cooper pairs. In most superconductors the Cooper pairs reside in the singlet state due to the Pauli principle. In the presence of an exchange field of a ferromagnet, the interaction tries to align the spins, thus destroying the superconductivity [7]. However, as long as the two-fermion correlation function is anti-symmetric under fermion exchange, then the Pauli-exclusion princple is satisfied and the Cooper pairs may reside in a triplet-spin state [1].

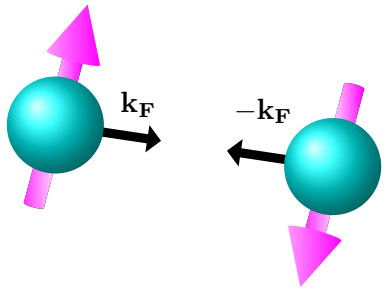

Figure 2.8: Cooper pairs are formed in the superconducting regime of material due to an attractive force between the electrons.

In FM/SC structures, Cooper pairs may penetrate into the FM and induce superconductivity there

via the proximity effect[34]. From spin mixing and spin rotation, odd frequency spin triplet Cooper pairs may be formed at the interface. As outlined by Jacob Linder and J.A. Robinson[1], scattering at the interface cause a shift in momentum and a spin-dependent shift in the wavefunction for the singlet Cooper pairs. The wave function starts out in the singlet state $|\psi\rangle_0 = \sqrt{1/2}(|\mathbf{k},\uparrow\rangle|-\mathbf{k},\downarrow\rangle - |\mathbf{k},\downarrow\rangle|-\mathbf{k},\uparrow\rangle)$ and the Zeeman field splits the spin carriers, thus causing the scattering. This produces a shift θ_σ, $\sigma\uparrow,\downarrow$ in the phase by the transformations $(|\mathbf{k},\uparrow\rangle \rightarrow e^{\theta\uparrow}|-\mathbf{k},\uparrow\rangle$ and $(|\mathbf{k},\downarrow\rangle \rightarrow e^{\theta\downarrow}|-\mathbf{k},\downarrow\rangle$. This produces a superposition of the singlet and the $S_z = 0$ spin triplet wavefunction, $|\psi\rangle_{even} = \sqrt{1/2}(|\mathbf{k},\uparrow\rangle|-\mathbf{k},\downarrow\rangle + |\mathbf{k},\downarrow\rangle|-\mathbf{k},\uparrow\rangle)$. In the presence of magnetic inhomogeneities, one of the spins may be rotated to form the $|\psi\rangle_{odd} = |\mathbf{k},\uparrow\rangle|-\mathbf{k},\uparrow\rangle, |\mathbf{k},\uparrow\rangle|-\mathbf{k},\uparrow\rangle$.

In NM/SC structures, the proximity effect changes both the properties of the NM and the SC. The superconducting condensate penetrates into the NM region over distances of the coherence length $\xi_N = \sqrt{D_{NM}/2\pi T}$, where D_{NM} is the classical diffusion coefficient. At low temperatures the coherence length increases and if it is greater than the thickness of the metal, the condensate encompasses the entire NM region [7].

CHAPTER 3: EXPERIMENTAL SETUP AND SAMPLE PREPARATION

The devices used in this study were two FMR integrated-coplanar waveguides (CPW). An FMR integrated CPW has the sample underneath the central line of the wave guide (Figure 3.1 and 3.2). The recipe for fabricating the devices was adopted from the del Barco group.

3.1 Device Fabrication

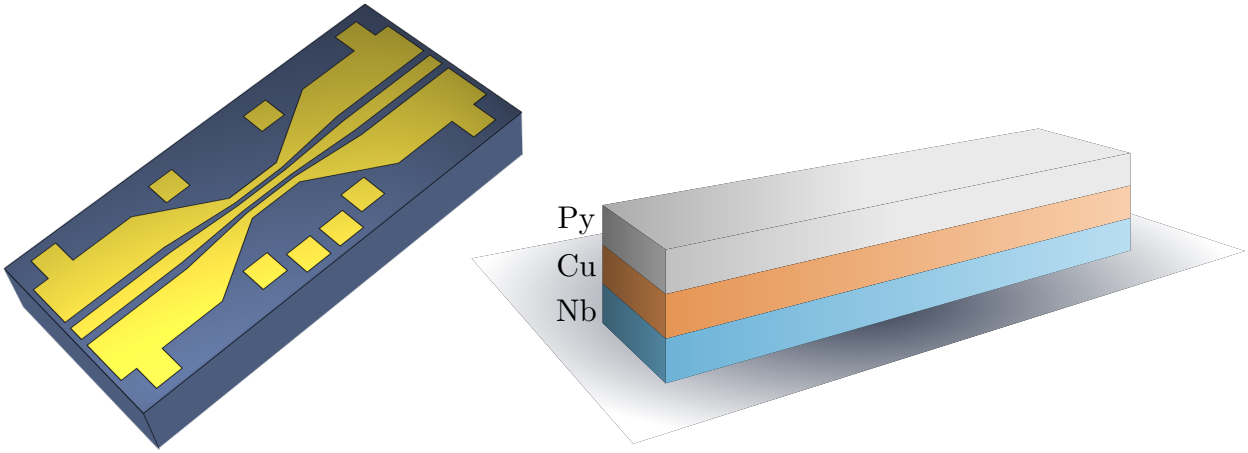

Figure 3.1: The integrated coplanar waveguide fabricated in the FMR experiments is seen on the left. Both Py and the Py/Cu/Nb stack depicted above both use the same design. Both the stacks lie underneath the central line of the waveguide. On the right, the Py/Cu/Nb stack that lies underneath the central line is 20 nm/10 nm/20 nm thick, respectively.

LOR-3A photo-resit was spin coated onto the GaAs wafer at 3000 rpm then baked on a hot plate at 175 °C for five minutes. This will form approximately a 1 μm thick layer of resist. A second layer of S1813 photo-resist was spun at 5000 rpm for 35 seconds then baked for 2 minutes at 115 °C. This forms approximately a 300 μm thick layer of resist on top of the 1 μm LOR.

Patterning is done by optical lithography. The pattern is laid down on the wafer using an optical

lithography mask inside of an UV mask aligner located in the clean room of the Physical Sciences Building (PSB) at the University of Central Florida (UCF). When placed in the mask aligner the patterned UV radiation was exposed to the resist for the amount of time it takes to reach 126 mJ/cm^2. The sample was then developed in CD-26 developer for 45 seconds to remove the exposed photoresist. After confirming the integrity of the pattern under a microscope, the wafer is hardened on a hot plate for 4 minutes at 130 °C. The wafer is then developed again in the CD-26 for 1 minute to perform an undercut on the LOR which will ease the liftoff state.

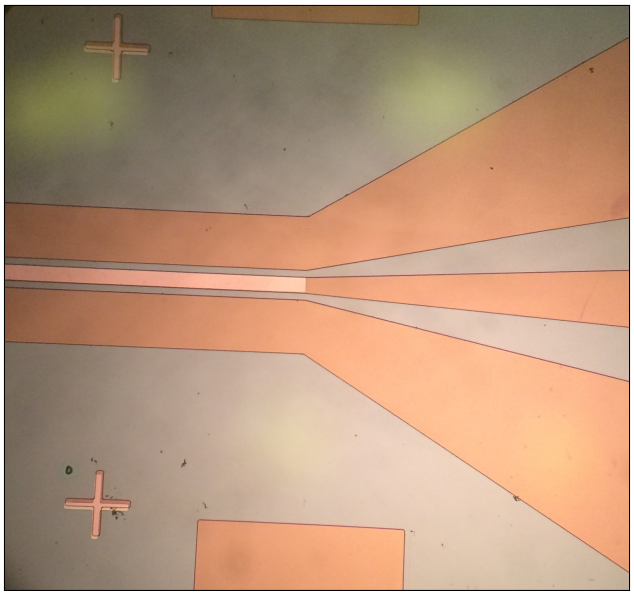

Figure 3.2: The alignment of the CPW on top of the Py/Cu/Nb sample. The crosses shown in the top and bottom left corners act as markers to carefully align the mask on top of the material.

The metal evaporation is done in an ultra-high vacuum (UHV) chamber. The deposition of the tri-layer was performed by Dr. Kevin Coffey's group in the Material Sciences department at UCF. For this particular stack, the layer thickness of the Py/Cu/Nb is 20nm/10nm/20nm, respectively. In order to prevent contact between the sample stack and the waveguide, 250 nm of silicon dioxide (SO_2) were evaporated on top of the entire wafer providing an insulating barrier between the two. For the CPW, the pattern is aligned cross hairs (shown on the left side of Figure 3.2) on the mask

and previous deposition to correctly position the sample underneath the mask. It is then developed and prepared for an evaporation in the UHV.

Prior to the metal deposition, the wafer is cleaned of any residue residing on the surface. This is done by plasma etching. Oxygen, O_2, at a flow rate of 12 standard cubic centimeters per minute (sccm) under a pressure of 200 mTorr was applied to the wafer in a Samco RIE etcher for 10 seconds. The metal is then placed inside the UHV which is pumped down to a base pressure of 5×10^{-6} Torr. The first layer of the wave guide consists of 7 nm of titanium (Ti) to provide a sticking layer to the wafer for the other metals. Prior to deposition, 10 nm was evaporated to remove the oxide layer for the Ti. The second layer was 200 nm of Cu-the main conductor. Similar to the Ti evaporation, 10 nm of Cu were evaporated prior to deposition to remove the oxide layer. A capping layer of gold (Au) of 10 nm was used to prevent oxidation of the Cu layer. Once out the chamber, the sample was placed in PG remover to perform the liftoff. This removed the photoresist and left the patterned metals. The second device was already prepared by a previous student in the clean room facilities at UCF.

3.2 Device Characterization

Device characterization shows the transmission of the FMR integrated CPW at room temperature and as a function of frequency. This provides detail to how much energy is transported into the device at a given frequency. The device was placed inside a non-magnetic brass housing box. This housing box consisted of 2.4 mm semi-rigid coaxial cables shaved at the ends and the center conductor of each cable goes through the holes on each side the housing box. The conductors made contact with the central line of the CPW. The grounds on the CPW were connected to the housing box using conductive silver paint as seen in Figure 3.3 (a).

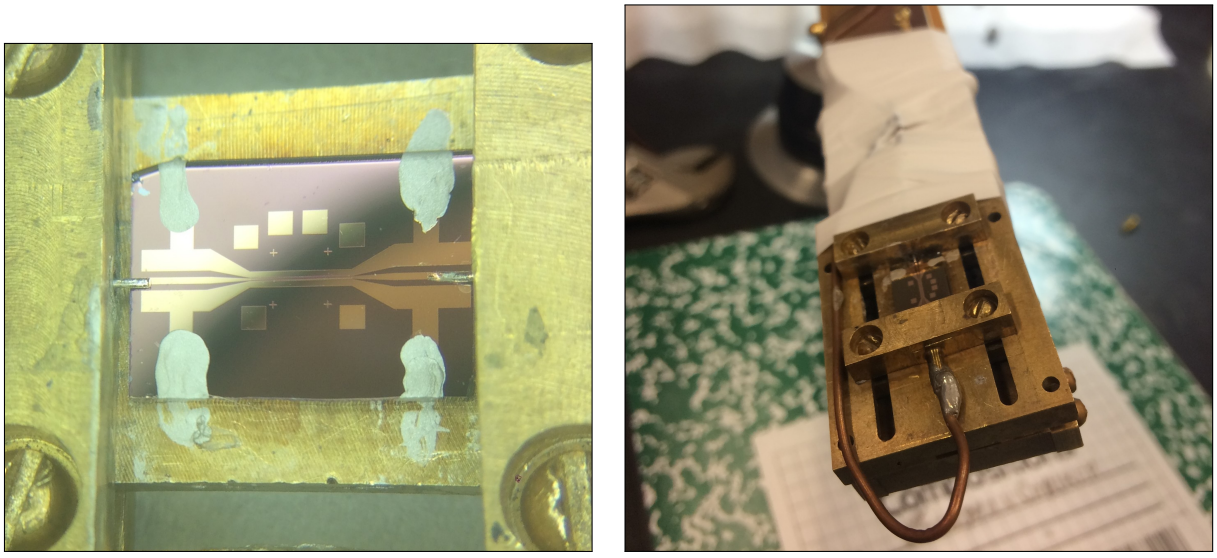

(a) (b)

Figure 3.3: (a) The FMR integrated CPW is placed inside of an adjustable housing box. The pins are aligned with the central line of the device using a working microscope. Silver paint grounds the sample to the housing box. (b) The housing box is mounted onto the ^{3}He cryostat. Screws (not shown) fix the housing box in place, and Teflon tape is used to wrap the wires around the coldfinger to prevent any motion.

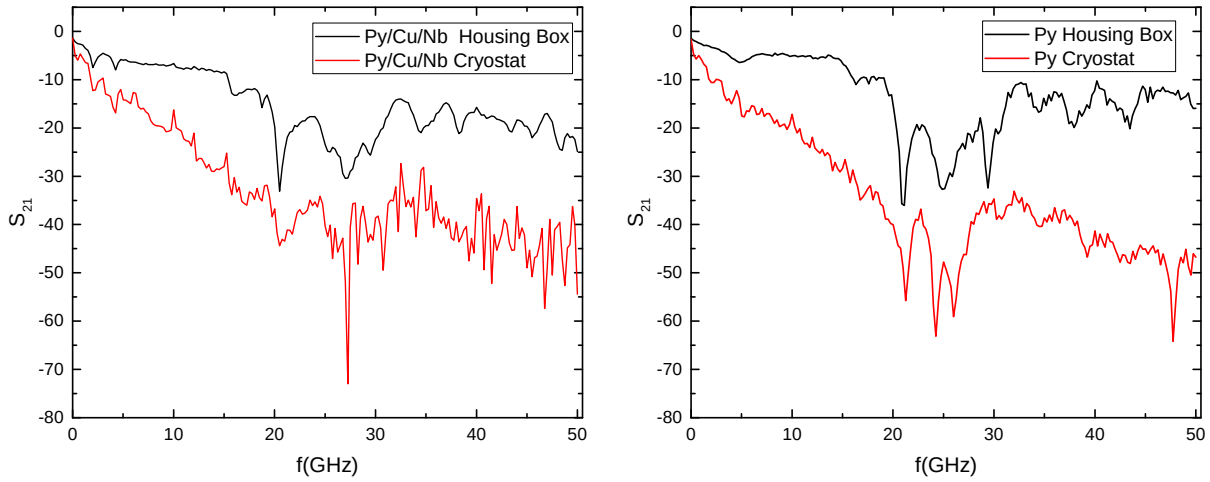

Figure 3.4: The transmission for both samples are shown depicting the loss of energy as a function of frequency. The black line represents the transmission of energy in only the housing box. The red line indicates the transmission through the housing box when connected to the cryostat. It is necessary to fix the frequency so that the minimal amount of energy is forfeited when measuring.

To perform the characterization, an Agilent Technologies Performance Network Analyzer (PNA) was connected to the housing box by the coaxial cables. The PNA sends microwave radiation through the two ports on the front panel. The PNA was first calibrated using the electronic calibration mode to account for losses and reflections existing in the lines connected to the PNA. The PNA was set to mode S_{21} which measures the energy difference being sent from Port 1 and received at Port 2. This analysis was also done when connected to the cryostat (mentioned in Section 3.3). The transmission for both devices at room temperature and low temperature in the cryostat can be seen in Figure 3.4.

3.3 FMR Measurements

The FMR measurements were carried out at low temperature of the range 2-14 K using an Oxford Insruments ^{3}He Cyrostat. The housing box containing the device was mounted on the cold-finger at the bottom of the cryostat as depicted in Figure 3.3(b). The cryostat was then mounted onto a hoist to raise the cryostat vertically. A lightweight vacuum hose line was attached to the inlet control valve (IVC) at the top of the cryostat; this is connected to a Leybold LH helium leak detector system. Inside the chamber resides the Sorbtion pump, which was heated prior to sealing to remove any present moisture. A brass cone was then cleaned with IPA, which covers the cold-finger. Industrial vacuum grease was applied around the IVC flange where the end of the brass sleeve reaches. The cone was slid up to the flange, where the cone was rotated while the IVC was evacuated with the turbo pump of the leak detector until a sufficient vacuum level for low-temperature measurements was achieved. This was allowed to pump down for $\sim$ 1 hour for each measurement.

Once the cryostat was pumped out, helium gas was used to check for leaks in the cryostat. Following this, a rubber helium gas line was attached to the leak detector and the leak detector was

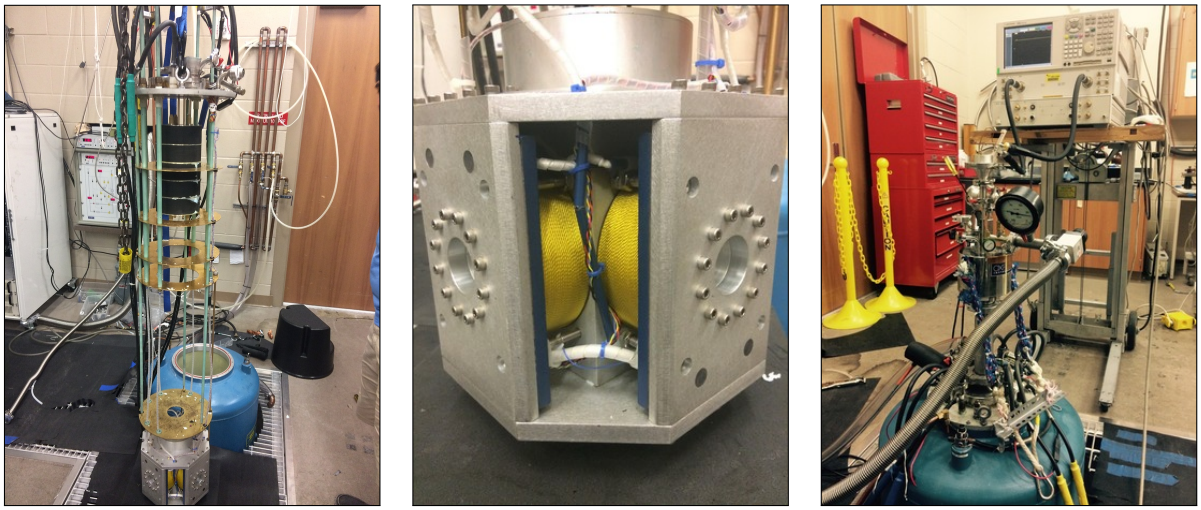

(a) (b) (c)

Figure 3.5: (a) The magnet has three leads at the top of the structure that are lowered to connect it to power. The internal rings allow the cryostat to be placed vertically inside. (b) The end of the cryostat is placed within the magnet located at the bottom of the dewar. (c) The cryostat is placed into the magnet and is connected to the PNA for FMR measurements.

placed in standby. Helium gas was then sent into the cryostat through the IVC valve-this will act as an exchange gas inside the cryostat to thermally couple the system to the outside envrionment. Gas flow was monitored with the needle valve on the cryostat. The cryostat was then placed inside the center of an American Magnetics three-axis superconducting magnet, seen in Figure 3.5(b). The magnet was contained within a dewar filled with liquid helium and an outer jacket containing liquid nitrogen.

FMR measurements are more practical when the microwave frequency is kept constant and the magnetic field is swept across the resonance condition. As explained in Section 2.1, FMR studies require an external field and an orthogonal a.c. magnetic field. The external field is generated by the superconducting magnet which is applied in the z-direction. Typically, there is an angle dependence on the FMR from the orientation of the magnetic field with respect to the a.c. magnetic field; however, the field along the z-axis is parallel to the cryostat, so the two fields were assumed

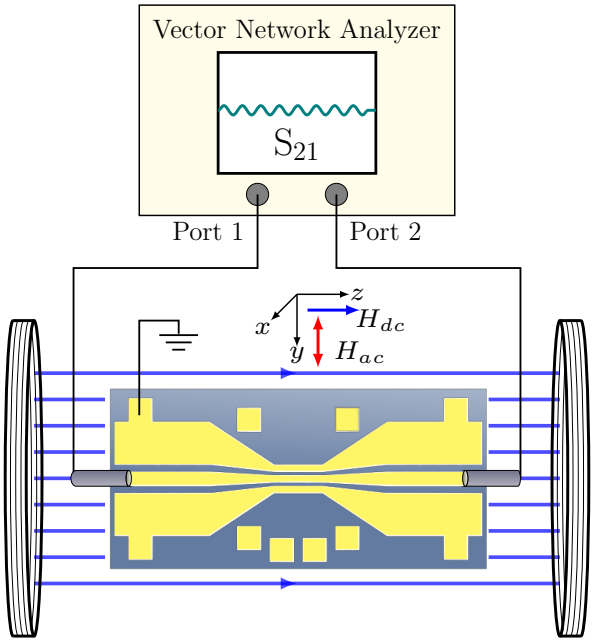

Figure 3.6: The PNA supplies microwave radiation through Port 2 and measures the amount received from Port 1. The microwaves generate an oscillating magnetic field. A dc magnetic field is applied perpendicular to the microwave to microwave radiation inducing spin pumping via FMR.

to be perpendicular.

A Labview virtual instrument (V.I.) was written prior to the experiment and was used to control the devices used in the experiment. The basic diagram of the measurements can be seen in Figure 3.6. The PNA supplies continuous wave microwave radiation at 8 GHz to the samples. The magnetic field is swept from 0 to 1.0 kilo-Gauss (kG) measuring the transmission of the device. The PNA collected 10 points over a 60 millisecond (msec) sweep time and the intermediate frequency (IF) bandwidth of the PNA was set to 150 Hz.

These measurements were carried out in the temperature interval 2-14 K. The temperatures were controlled using an Oxford Instrument intelligent temperature controller. By setting temperatures on the temperature controller, the temperature was increased in small intervals of approximately 0.25 K until the temperature reached 7 K. After 7 K, the intervals increased to 0.50 K until 14

K was reached. The resonance spectrum of the Py/Cu/Nb sample at 2K, as well as its calculated derivative, can be seen in Figure 3.7. The results for both samples are discussed in chapter 4.

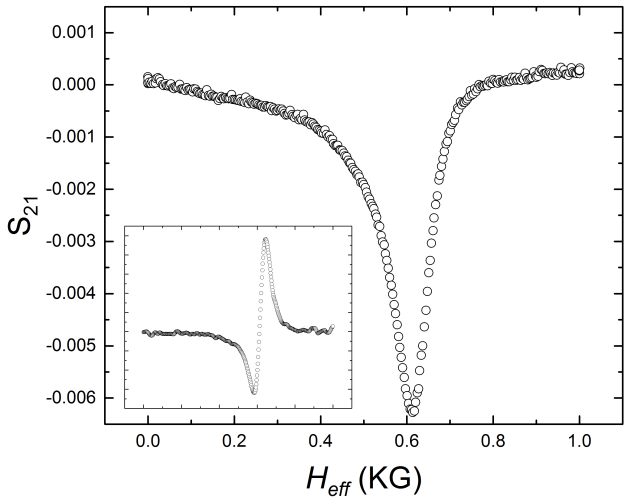

Figure 3.7: The FMR spectrum for the Py/Cu/Nb sample carried out at 2 K. The derivative of the FMR signal is seen in the lower corner. The peak to peak separation of the derivative is know as the linewidth ΔH and provides information about the damping in the material due to spin pumping.

CHAPTER 4: RESULTS

4.1 Py/Cu/Nb Measurements

The transmissions and derivatives of both the Py/Cu/Nb and Py samples were constructed in contour plots to visualize the temperature dependence of damping in both the normal state and superconducting state. The FMR spectrum can be seen in Figure 4.1. There is evidence of abnormal behavior in the FMR around 7-8 K, which is attributed to the superconducting to normal conducting transition. The resonance field seems to change as well, i.e. shift with temperature. There is also an increase in the amplitude of the observed FMR signal at lower temperature than higher temperature suggesting a decrease in damping.

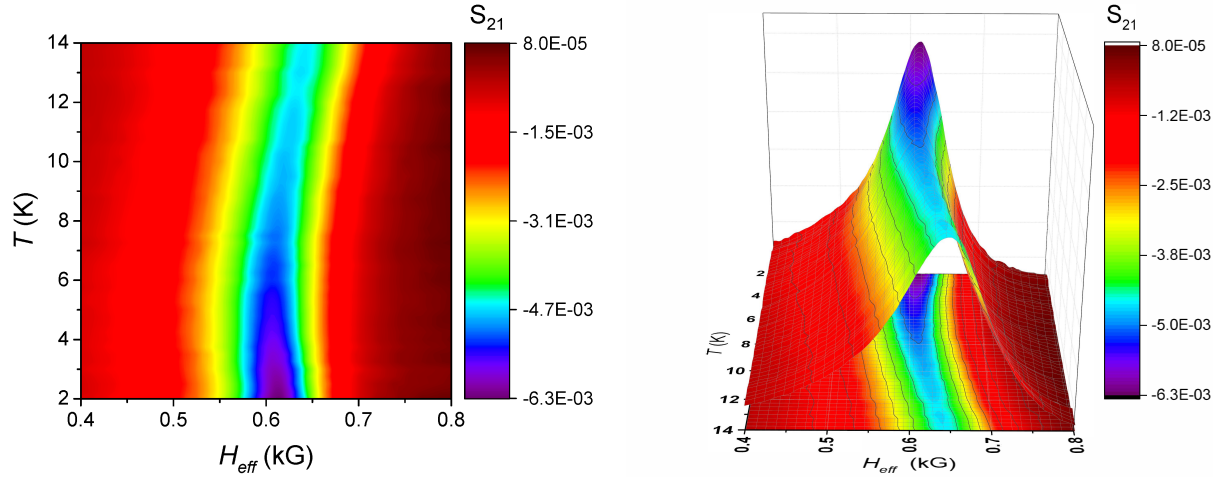

Figure 4.1: (a) The FMR contour plot for Py/Cu/Nb. The scale shown shows minimum transmission for red and maximum transmission for violet. (b) The FMR projection for the Py/Cu/Nb device. Note the temperature and transmission scales are inverted in the projection for an improved observation of the behavior of the FMR signal.

To understand the effective spin pumping into the sample, the derivative of the FMR spectrum is

taken with respect to the field, H_{eff}. It can been seen in Figure 4.2 that the derivative moves with changes in temperature. The rate of change in the shape of the signal is also very large at lower temperature. As the temperature increases, the magnitude decreases and peak to peak separation increases.

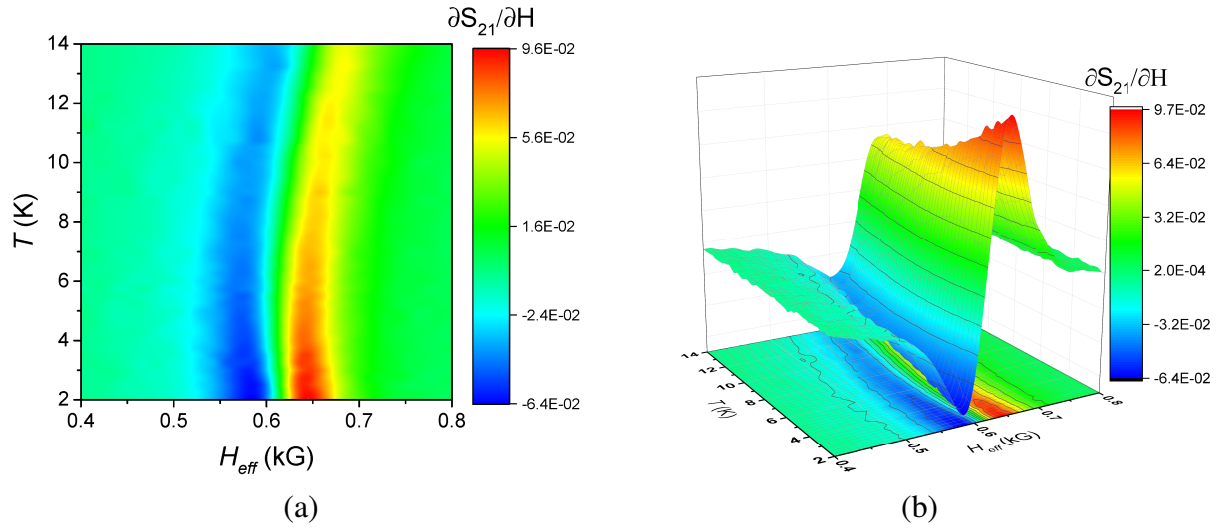

Figure 4.2: (a) The derivative of the FMR signal for the Py/Cu/Nb CPW. (b) The projection of the derivative.

The main parameters extracted are the effective change in the linewidth, ΔH, and the field at which resonance occurs, H_r. The peak to peak separation of the derivatives provide the linewidth, that is $\Delta H = H_1 - H_2$, where H_1 and H_2 are the strength of the two fields measured at each peak. H_r is found by taking the average distance between the two peaks, the resonance essentially lies where the derivative is zero, that is $H_r = (H_1 + H_2)/2$. The results can be seen in Figure 4.3.

It is obvious that there is a significant change in the behavior of the sample below $T = 8$ K. In Figure 4.3(a), the width decreases at a constant rate, and then between 7-8 K the rate at which the width decreases chanes. This can be observed by the two lines indicating the different rates. In Figure 4.3(b), the resonance behaves differently around the same temperature for the anomoly in Figure 4.3(a). The resonance field decreases with temperature at a linear rate, but it begins to

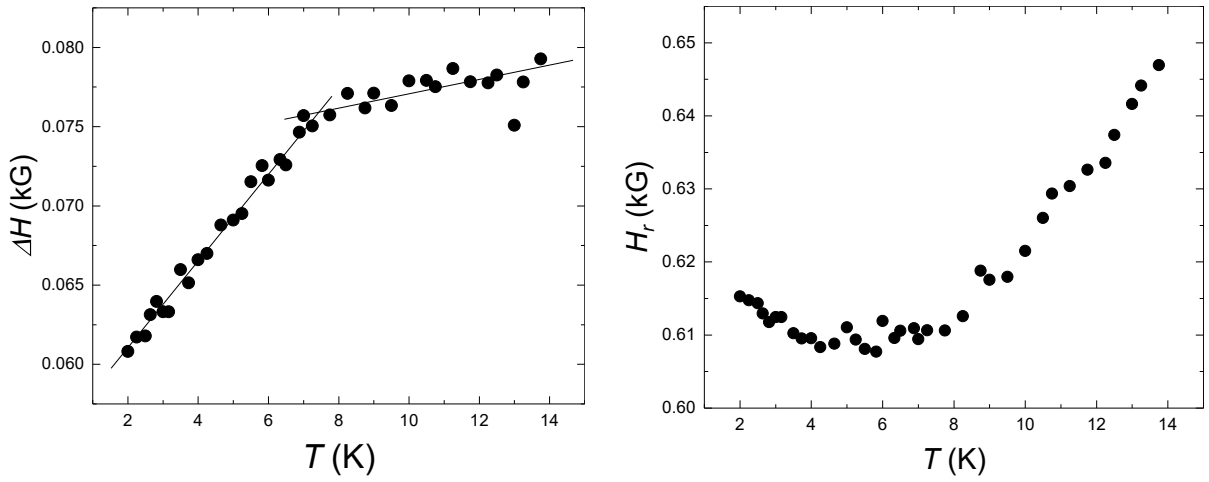

Figure 4.3: (a) The change in damping of the Py/Cu/Nb sample as a function of temperature. The fit is to help guide the eyes. (b) The field of resonance shifts to lower field as temperature increases but then begins to change direction.

veer and begin to reverse direction. The minimum H_r occurs somewhere around 6 K, and then H_r increases below that temperature.

4.2 Py Measurements

The results for the Py FMR spectrum can be seen in Figure 4.4. The amplitude of Py changes very quickly below 5 K then slowly decreases. As the temperature increases, the resonance field shifts to the right. The derivative for the Py sample can be seen in Figure 4.5. For temperatures above 5 K, the peaks of the derivative become very small with respect to the ones below 5 K. This expresses the dramatic decrease in amplitude of the resonance peak in Figure 4.4.

The extracted information from the Py measurements can be seen in Figure 4.6. As the temperature increases, the linewidth increases. There is no observed change in the width of the sample as it is linear up to 7 K then becomes very noisy. However, a linear relationship between linewidth and

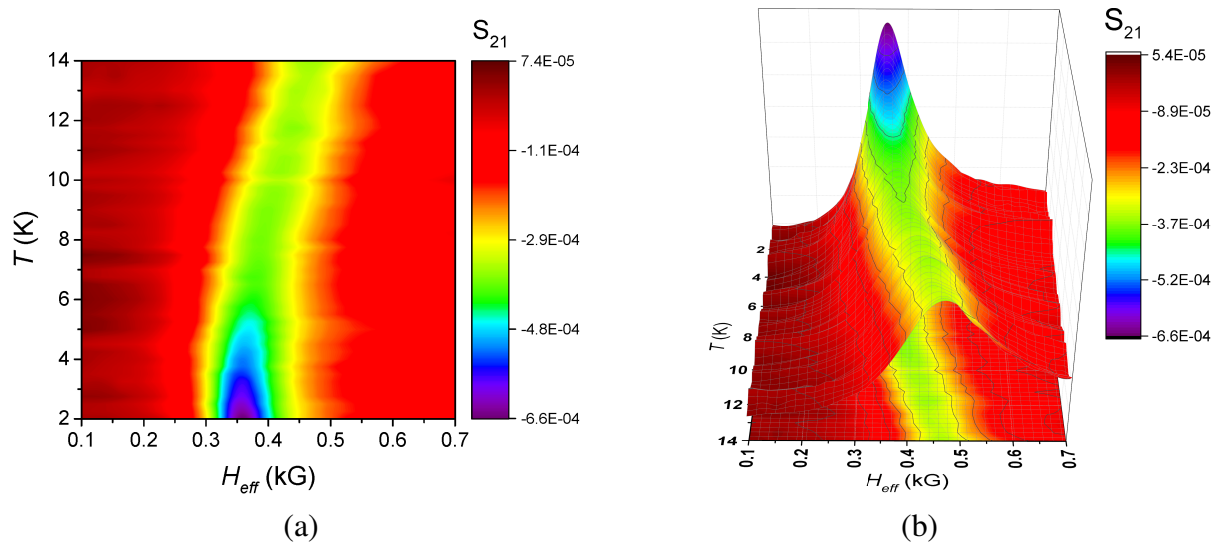

Figure 4.4: (a) The FMR contour plot for the Py sample. (b) The FMR projection for the Py sample.

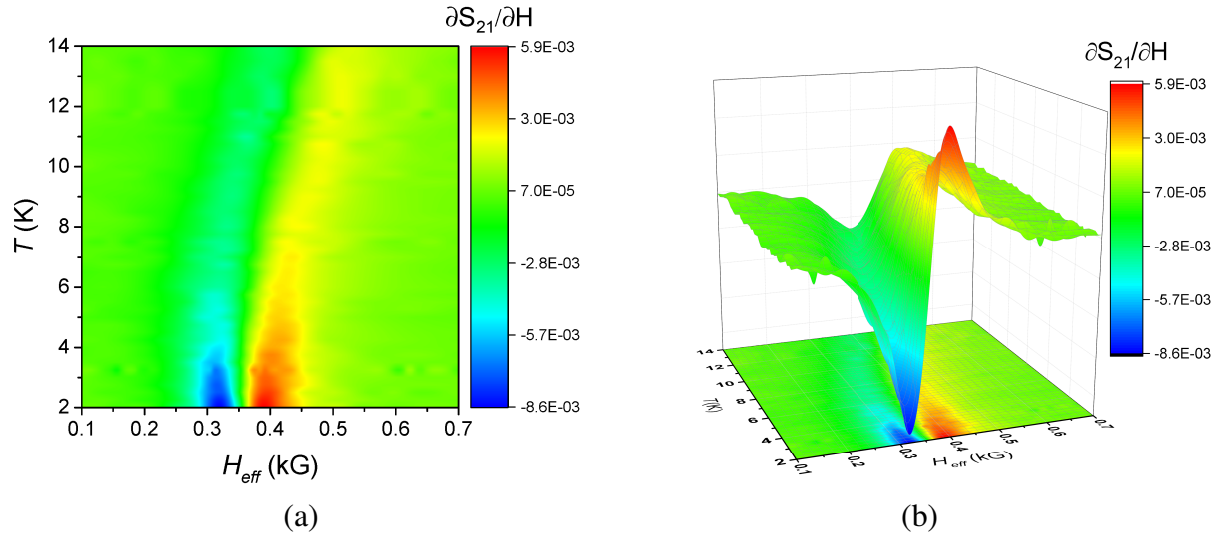

Figure 4.5: (a) The contour plot of the derivative with respect to H for the Py sample. (b) The projection of the derivative.

temperature for a Py sample agrees with previous works [14]. Also, the resonance shifts to smaller field as the temperature decreases. At around 3 K, the resonance field seems to stay constant down to 2 K.

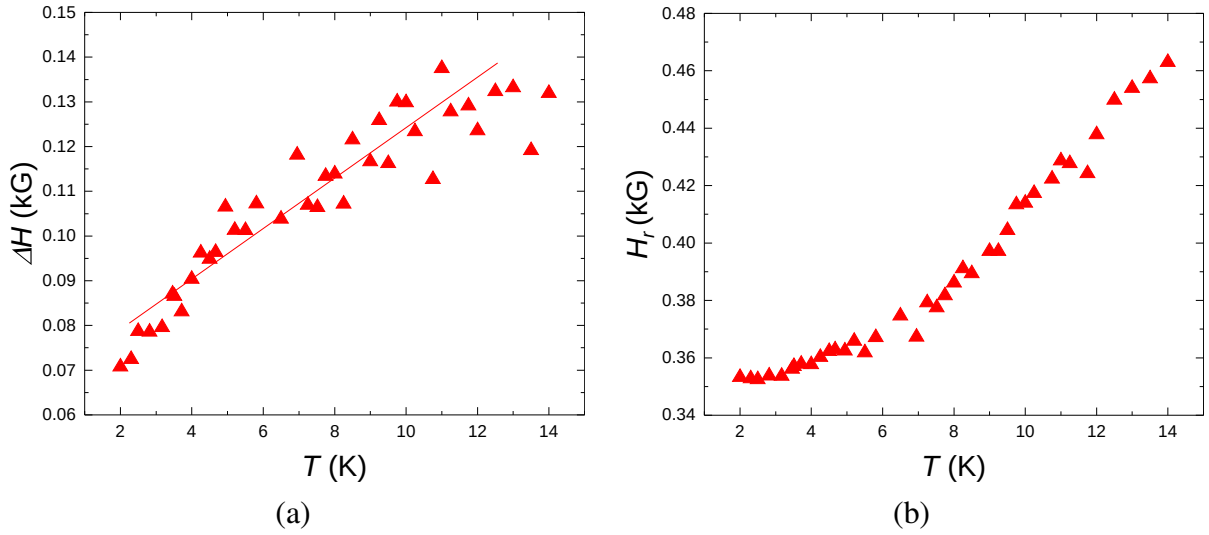

Figure 4.6: (a) The observed change in damping for the Py sample. As temperature decreases, the width decreases. (b) The observed field at which resonance occurs for the Py sample. As temperature decreases the resonance shifts to lower field until about 3 K, where it seems to remain constant.

4.3 Analysis

In this section, comparative analysis of the results obtained in the Py/Cu/Nb and Py samples is presented. The interpreted differences are correlated to the direct effect of the material in the superconducting state restricting the absorption of spin angular momenta from the ferromangetic Py film.

By shifting the derivative to zero, the way the width behaves becomes more clear as seen in Figure 4.7. Figure 4.7(a) and Figure 4.7(b) display the derivatives of the normalized FMR signal shifted by the resonance of each temperature for the Py/Cu/Nb and Py samples, respectively. For the

Py/Cu/Nb sample, it is apparent that the peaks do not behave the same. As T increases from 2 K, the left peak begins to shift towards lower field at a constant rate. The right peak moves at a constant rate then shifts around 7 K with a new constant rate. The intermediate step between 7-9 K may be due to noise in the measurements. Albeit, the peak to peak behavior of the Py/Cu/Nb poses interesting questions about the mechanisms behind them. It suggests the possibility of superconductive influence only after the resonance condition is met.

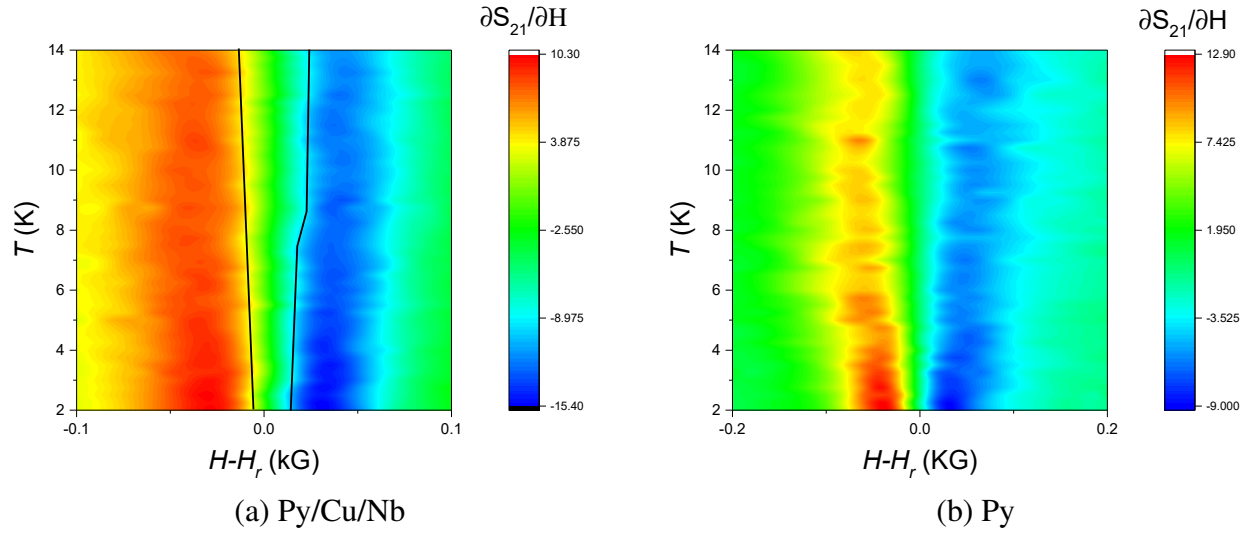

(a) Py/Cu/Nb (b) Py

Figure 4.7: The contour plot of the derivative of (a) the Py/Cu/Nb and (b) the Py samples. Both were taken from the normalized FMR signal with the field of resonance subtracted at each temperature.

The manner in which the width behaves for increasing temperature as seen in Figure 4.7(b), displays a considerable amount of noise. It does display a monotonous increase in width up to about 11 K, which is different to that observed in the Py/Cu/Nb samples. A recent study showed that as temperature decreases from room temperature, the linewidth in FMR measurement in Py based systems increases [36]. Some studies have shown that the increase in linewidth may be attributed to an oxidation layer on the Py layer as opposed to when it is capped with Cu where no temperature dependence is observed [35]. In a similar study, FMR induced spin pumping in a cobalt/platinum bilayer showed a similar increase in linewidth up to 30 K, where it reaches a maximum and then

began to decrease with decreasing temperature [35]. The noise in the Py sample measurements may be attributed to noise from the CPW. Good electrical contact is needed between the pins of the housing box and the CPW for a clean signal. It's possible that the PNA may have contributed to the noise is possible given that the Port 2 showed signs of malfunction after this experiment.

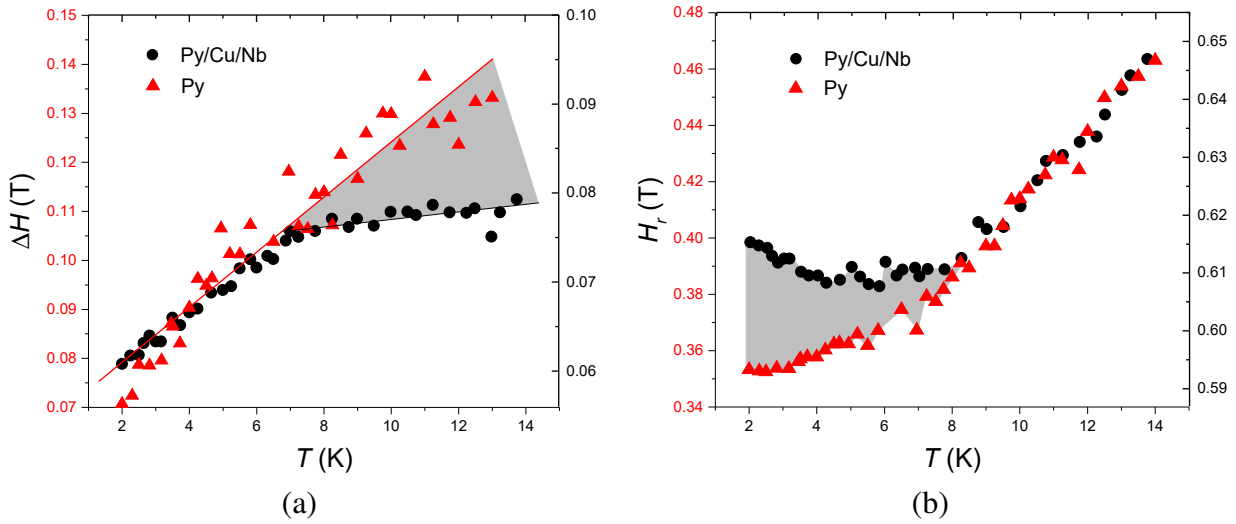

Figure 4.8: (a) The changes in ΔH for the Py and the Py/Cu/Nb sample. (b) The resonance field for both sample. The respective axis for each sample are indicated by their color.

Figure 4.8(a) shows the temperature dependence of ΔH of the Py and Py/Cu/Nb samples in their respective scales. The figure is plotted in this manner to show how both samples behave as temperature increases by avoiding the difference in magnitude. A linear fit for the Py displays a slope similar to the linear fit for the Py/Cu/Nb sample below 8 K. Once above 8 K, a different linear fit is used to show the rate of increase in linewidth. The two linear fits of the Py/Cu/Nb sample intersects at approximately 7 K. Because the slope of the Py/Cu/Nb sample matches the Py sample, this suggests a suppression of spin pumping in the Py/Cu/Nb sample. Since the Py/Cu/Nb sample behaves similarly to Py sample (the slopes are approximately the same), this implies the Nb layer does not absorb spin angular momenta from the Py layer in its superconducting state.

The transition temperature for the Py/Cu/Nb sample has yet to been measured, so only the behavior

below and above the suspected region of phase transition is discussed. The greater ΔH seen in the Py sample may be attributed to its thickness as damping increases inversely proportionally to thickness [35]. Raposo et al. reported FMR measurements as a function of temperature in Py structure line-arrays where the resonance field decreases with temperature from room temperature to 85 K. The decrease in width was attributed to the decrease in the saturation magnetization with the temperature due to the small value of the anisotropy constant [36]. This is not the case in the Py/Cu/Nb sample and it is still not understood.

Figure 4.8(b) shows the temperature dependence of the resonance field, H_r, for the two samples. In the case of the Py sample, the resonance field shifts monotonically to lower fields as the temperature decreases. This is different in the case of the Py/Cu/Nb sample, which shows a clear non-monotonic behavior starting at temperatures below 7-8 K. This behavior is ascribed to the transition into the superconducting state.

CHAPTER 5: SUMMARY AND OUTLOOK

The study of temperature dependent magnetization dynamics in a superconductor showed intriguing results. The resonance behaves differently than what has been reported in other systems. The clear non-monotonic behavior of the resonance field below 7-8 K in the Py/Cu/Nb sample suggests the effect of superconductivity on the magnetic properties of the Py layer. The different slopes for ΔH vs. T in the Py/Cu/Nb sample suppression of the spin sinking mechanism due to the formation of Cooper pairs in agreement with the theory. In a previous work done by Bell et. al [14], they reported a sudden jump in damping at the transition temperature for a Py/Nb sample which is not the case for the Py/Cu/Nb sample. This indicates that the copper spacer may have some influence on the spin dynamics of the sample by eliminating the direct proximity effects between the superconducting and ferromagnetic layers.

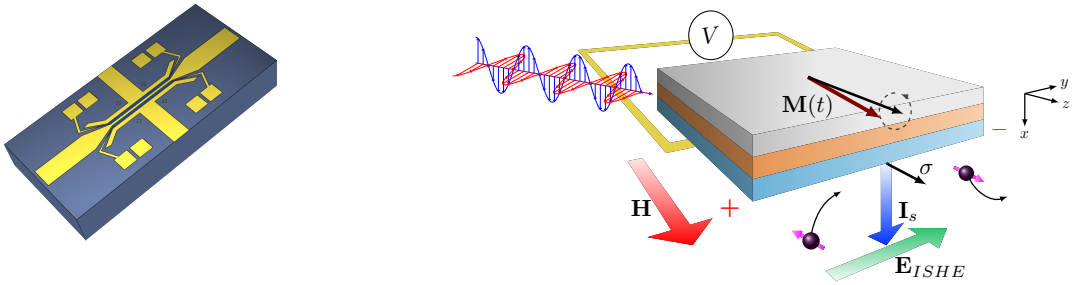

(a) (b)

Figure 5.1: (a) The ISHE device used to measure the Hall voltage at low temperatures. (b) The schematic diagram of the ISHE in the tri-layer. Spin current is pumped into the Nb from the Py by dynamical spin injection. This creates an electromotive force aligning the electrons in Nb to the lateral side of the sample along the y-axis. $\mathbf{H}$, $\mathbf{M}$, $\mathbf{E}_{ISHE}$, $\boldsymbol{\sigma}$, $\mathbf{I}_s$ are the effective field, the precessing magnetization, the electromotive force from the Hall votlage, the spin polarization vector, and the injected spin current, respectively.

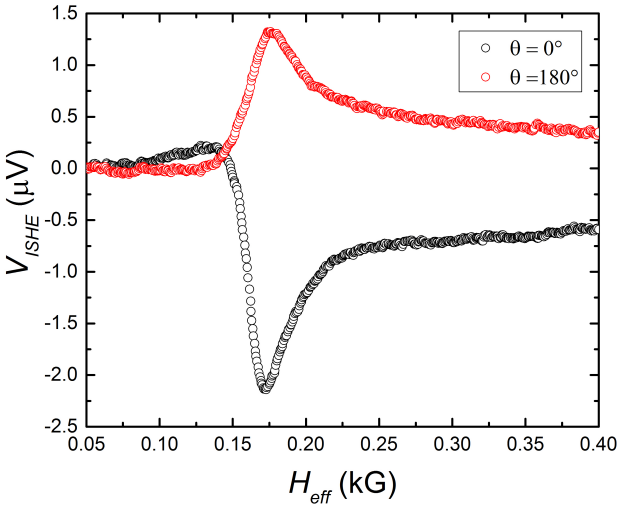

Figure 5.2: The voltage generated from the ISHE in the Py/Cu/Nb sample at room temperature.

Oxidation effects pose important questions in temperature dependent thin film systems as there is not much reported on the subject [35]. Capping the Py layer with a very poor spin sink could lead to understanding the consequences of an oxidation layer in FM. The interface between the SC and FM pose temperature dependent FMR questions. Although it was reported by Bell et al. [14] that the superconducting state suppresses spin sinking deficiency, there was no report on the resonance or magnetization properties of the Nb/Py sample. This presents an interesting study for measuring magnetic properties of thin-film systems in the superconducting state.

For a FM/NM/SC system, it was shown that different frequencies of radiation have an effect on the formation of odd frequency Cooper pairs which are able to absorb spin angular momentum [13]. Another study can be done by performing temperature sweeps at different frequencies to observe the change in damping. The observed enhanced ISHE from the NbN sample begs the question of measuring the ISHE by spin pumping [5]. Following this experiment, we expect to measure the ISHE of a Py/Cu/Nb stack in the superconducting regime. The device for the ISHE is shown in Figure 5.1(a). I have already measured the ISHE effect at room temperature for the Py/Cu/Nb

stack. The signal can be seen in Figure 5.2. Rotation of the magnetization 180° demonstrates the reversal of the signal showing evidence of the SHE in the Py/Cu/Nb stack.

To completely understand the physics of spin pumping at FM/SC interfaces, we are planning to reproduce the studies present in this thesis with Py, Py/Cu, Py/Nb and Py/Cu/Nb samples grown under the same exact conditions. We will also expand the FMR studies with measurements of the ISHE at low temperatures to evaluate the effect of transition into the superconducting regime in Nb and possibly other materials.

LIST OF REFERENCES

[1] J. Linder and J. Robinson, Superconducting Spintronics, *Nature Physics* **11**, 307315 (2015).

[2] I. Zutic, J. Fabian, and S. Das Sarma, Spintronics: Fundamentals and applications., *Rev. Mod. Phys.* **76**, 323 - 409, (2004).

[3] O. Mosendz, V. Vlaminck, J. E. Pearson, F. Y. Fradin, G. E. Bauer, S. D. Bader, and A. Hoffmann, Detection and quantification of inverse spin Hall effect from spin pumping in permalloy/normal metal bilayers, *Phys. Rev. B* **82**, 214403 (2010).

[4] A. Patra, B. S. Singh, Y. L. Barin, J.-H. Ahn, E. d. Barco, E. Mucciolo and B. zyilmaz, Dynamic Spin Injection into Chemical Vapor Deposited Graphene, *Appl. Phys. Lett* **101**, 162407 (2012).

[5] T. Wakamura, H. Akaike, Y.Omori, Y.Niimi, S. Takahashi, A.Fujimaki, and Y. Otani, Quasiparticle-mediated spin Hall effect in a superconductor, *Nature Materials* **14**(7), 675-+ (2015).

[6] Y. Izyumov, Y. Proshin and M. Khusainov, Competition between superconductivity and magnetism in ferromagnet/superconductor heterostructures *Physics-Uspekhi*, **45**(2), 109-148 (2002).

[7] F. Bergeret, A. Volkov and K. Efetov, Odd triplet superconductivity and related phenomena in superconductor-ferromagnet structures, *Reviews of Modern Physics* **77**(4), 1321 (2005).

[8] F. Bergeret and I. Tokatly, Spin-orbit coupling as a source of long-range triplet proximity effect in superconductor-ferromagnet hybrid structures, *Phys. Rev. B* **89**, 134517 (2014).

[9] K. Ohishini, T. Kimura and Y. Otani, Nonlocal injection of spin current into a superconducting Nb wire, *App. Phys. Lett* **96**, 192509 (2010).

[10] N. Poli, J. P. Morten, M. Urech, A. Brataas, D. B. Haviland , and V. Korenivski, Spin injection and relaxation in a mesoscopic superconductor, *Phys. Rev. Lett* **100**, 136601 (2007).

[11] K. Ohnishi, Y. Ono, T. T. Nomura and T. Kimura, Significant change of spin transport property in Cu/Nb bilayer due to superconducting transition, *Scientific Reports*, **4**, 6260 (2014).

[12] Bell, C., Loloee, R., Burnell, G., and Blamire, M. G., Characteristics of strong ferromagnetic Josephson junctions with epitaxial barriers, *Phys. Rev. B* **71**, 180501(R) (2005).

[13] Yokoyama, T., and Tserkovnyak, Y., Tuning odd triplet superconductivity by spin pumping. *Phys. Rev. B* **80**, 104416 (2009).

[14] C. Bell, S. Milikisyants, M. Huber and J. Aarts, Spin dynamics in a superconductor-ferromagnet proximity system, *Physical Review Letters* 100(4), (2008).

[15] T. Wakamura, N. Hasegawa, K. Ohnishi, Y. Niimi and Y. Otani, Spin Injection into a Superconductor with Strong Spin-Orbit Coupling, *Physical Review Letters* **112**(3), (2014).

[16] R. A. Klemm, *Layered Superconductors*. Oxford : Oxford University Press, (2012).

[17] O. Yaln, *Ferromagnetic Resonance Theory and Applications*, InTech 978-953-51-1186-3 (2013).

[18] S. V. Vonsovskii, *Ferromagnetic Resonance*, Pergamon Oxford (1966).

[19] T. Taniguchi and H. Imamura, Spin Pumping in Ferromagnetic Multiplayers, *Modern Physics Letters B* **22**(30), 2909-2929 (2008).

[20] A. Brataas, Y. Tserkovnyak, and G. W. Bauer, Scattering Theory of Gilbert Damping, *Phys. Rev. Lett.* **101**, 037208 (2008).

[21] Y.Tserkovnyak, A. Bratass and G. Bauer, Spin pumping and magnetization dynamics in metallic multilayers, *Phy. Rev. B* **66**, 224403 (2002).

[22] Y. Tserkovnyak, A. Brataas, G.E.W. Bauer, and Halperin, B. I., Nonlocal magnetization dynamics in ferromagnetic heterostructures, *Reviews of Modern Physics*, **77**(4), (2005).

[23] Y. Tserkovnyak, A.Brataas, and G. W. Bauer, Dynamic exchange coupling and Gilbert damping in magnetic multilayers (invited), *Journal Of Applied Physics* **93**(10), 7534 (2003).

[24] C. Boone, H. Nembach, J. Shaw and T. Silva, Spin transport parameters in metallic multilayers determined by ferromagnetic resonance measurements of spin-pumping, *Journal of Applied Physics* **113**(15), 153906 (2013).

[25] S. Singh, M. Anguera, E. del Barco, R. Springell and C. Miller, Moderate positive spin Hall angle in uranium., *App. Phys. Lett.* **107**(23), 1-5 (2015).

[26] K. Ando, and E.Saitoh, Inverse spin-Hall effect in palladium at room temperature. *Journal Of Applied Physics* **108**(11), 113925-1-113925-4, (2010).

[27] J.J. Sakurai, and .S.F. Tuan, *Modern Quantum Mechanics: Revised Edition*, Pearson Eduction, (2002).

[28] T. Yoshino, Y. Kajiwara, K. Ando, H. Nakayama, T. Ota, K. Uchida and E. Saitoh, Detection of inverse spin-Hall effect in Nb and $Nb_{40}Ti_{60}$ thin films, *Journal of Physics: Conference Series* **200**(6), 062038, (2010).

[29] E. Saitoh, M. Ueda, H. Miyajima and G. Tatara, Conversion of spin current into charge current at room temperature: Inverse spin-Hall effect, *Appl. Phys. Lett* **88**, 182509 (2006).

[30] M. Morota, Y. Niimi, K. Ohnishi, T. Tanaka, H. Kontani, T. Kimura, and Y. Otani, Indication of intrinsic spin Hall effect in 4d and 5d transition metals, *Phys. Rev. B* **83**, 174405, (2010).

[31] M.I Dyakonov and V.I. Perel, V.I. Current-induced spin orientation of electrons in semiconductors, *Phys. Lett. A* **35** , 459-460 (1971).

[32] M.I. Dyakonov and V. I. Perel, "Possibility of orientating electron spins with current", *Sov. Phys. JETP Lett* **13**, 467 (1971).

[33] Y.K. Kato, R.C. Meyers, A.C. Gossard, and D.D. Awschalom, Observation of the Spin Hall Effect in Semiconductors. *Science* **306**, (5703) (2004).

[34] A. I. Buzdin, Proximity effects in superconductor/ferromagnet heterostructures. *Rev. Mod. Phys.* **77**, 935-975 (2005).

[35] T. A. Verhagen, H. N. Tinkey, H. C. Overweg, M. van Son, M. Huber, J. M. van Ruitenbeek, and J. Aarts, Temperature dependence of spin pumping and Gilbert damping in thin Co/Pt bilayers. *Journal Of Physics. Condensed Matter: An Institute Of Physics Journal* **28**(5), 056004 (2016).

[36] V. Raposo, A. Flores, M. Zazo, J. Iiguez, C. Redondo, and D. Navas, Temperature dependence of ferromagnetic resonance measurements in nanostructured line arrays. *EPJ Web Of Conferences* **75**, 05016 (2014).